Available online at www.sciencedirect.com

ScienceDirect

journal homepage: http://www.elsevier.com/locate/acme

Original Research Article

Tensile behavior, microstructure, and substructure of the friction stir welded 70/30 brass joints: RSM, EBSD, and TEM study

Akbar Heidarzadeh

Department of Materials Engineering, Azarbaijan Shahid Madani University, Tabriz, Iran

ARTICLE INFO

Article history:
Received 12 June 2018
Accepted 30 September 2018
Available online 13 October 2018

Keywords:
Friction stir welding
Strength
Elongation
EBSD
TEM

ABSTRACT

The effect of bead on plate friction stir welding parameters on the tensile properties of the 70/30 brass joints was investigated using response surface method. The microstructures of the joints were characterized using optical microscopy, electron backscattered diffraction (EBSD), and transmission electron microscopy (TEM). The tensile test was conducted to measure the ultimate tensile strength and elongation of the joints. In addition, the fracture surfaces of the tensile specimens were analyzed by scanning electron microscopy (SEM). The results showed that the most effective parameters on the strength and elongation of the joints were tool rotational speed and axial force, respectively. Optimizing the parameters revealed that the maximum strength and elongation of 318.5 MPa and 54.9% can be achieved at a rotational speed of 1000 rpm, a traverse speed of 58.4 mm/min, and an axial force of 3 kN. The strengthening mechanisms of grain boundary and dislocation density effects were responsible for the higher ultimate tensile strength of the joints welded at the lower heat input conditions. Furthermore, the effect of friction stir parameters on the ultimate tensile strength and elongation of the joints has been discussed, thoroughly.

1. Introduction

The brasses (Cu–Zn alloys) have different physical and mechanical properties according to their Zn content. Therefore, a wide range of properties can be achieved in brasses by changing their chemical composition. In addition, brasses have high electrical and thermal conductivities, high corrosion resistance, good combination of strength and ductility, etc. [1]. These various properties of brasses have attracted many attentions in both the academic and industrial point of views. Thus, the demands have been increased for manufacturing and processing of the brass parts. One of the most important processes is welding and joining during production of brass parts.

Unfortunately, the conventional fusion welding processes are not suitable for joining the brasses, which is due to two major reasons. First, the high thermal conductivity of the brasses cause the need for high heat inputs during fusion welding processes, and hence wide heat affected zone (HAZ) can be formed in the structure of the joints. Second, fusion and solidification of the weld metal results in dendritic structures, macro and micro segregations, porosities, inclusions, shrinkages, large distortions, residual stresses, zinc evaporations,

E-mail addresses: ak.hz62@gmail.com, ac.heydarzadeh@azaruniv.ac.ir.
https://doi.org/10.1016/j.acme.2018.09.009

color change, etc. in the joints [2]. These difficulties of the conventional fusion welding have encouraged the scientists to find new methods for joining the brasses.

Fortunately, it has been proved by researchers that the friction stir welding (FSW) is a suitable method to join the brasses [3,4]. In this process, a rotating non-consumable tool inserts into the work pieces and then traverses along the welding line. During FSW, the materials do not melt, in which the coexistence of heat and severe plastic deformation leads to sound joint formation. Thus, the conventional fusion welding problems, arisen from the melt and solidification steps, are eliminated by using FSW. On the other hand, the FSW joints have a deformed and recrystallized structure, which typically causes enhancement of the mechanical properties [5,6]. Thus, FSW can be a promising method to replace the conventional fusion methods for joining the brasses.

Some researchers have studied the FSW of brasses in recent years [7–15]. Heidarzadeh et al. [7] have compared the microstructure and mechanical properties of the single and double phase brass alloys, and found that the double phase joint had finer grain structure and better mechanical properties. Wang et al. [8] have used water flowing during FSW of Cu–30 wt.% Zn, which caused formation of grains inside the SZ of the joints with an average size smaller than 1 μm. Heidarzadeh et al. [9] have correlated between process parameters, grain size, and hardness of friction-stir-welded Cu–Zn alloys. They showed that the Hall–Petch equation deviates from its linear relationship due to formation of substructures inside the stir zone (SZ). Mironov et al. [10] have investigated the grain structure formation during FSW of Cu–30 wt.% Zn alloy. They demonstrated that the new grains form by bulging of the grain boundaries and nucleation mechanism during FSW, which causes finer grain sizes and high strengths in the joints. Xie et al. [11] have studied the effects of FSW parameters on microstructures and mechanical properties of brass joints. They showed that the tensile and yield strengths of the welds reached up to ~99 and 80% of the PM, respectively. In Ramesh et al. [12] research, the 6-mm-thick dual-phase brass plates were joined efficiently using FSW at various tool rotational speeds. They concluded that the recrystallization was inhomogeneous in SZ and the inhomogeneity reduced with increased tool rotational speed. Heidarzadeh et al. [13] investigated the Microstructure, texture, and mechanical properties of friction stir welded commercial brass alloy. They revealed that continuous and discontinuous dynamic recrystallizations (CDRX and DDRX) were the main mechanisms of the grain structure formation during FSW. Ozer et al. [14] explored the effect of FSW parameters on microstructure and fatigue strength of Cu–37 wt.% Zn brass alloys. Liu et al. [15] have studied the microstructural evolution during FSW of a single phase brass. They have shown DDRX in conjunction with annealing twinning are the grain structure formation during FSW.

According to the above literature, some researchers have investigated FSW of brass plates. However, an investigation into the optimizing the process parameters in conjunction with elucidating the origins of the improved mechanical properties in the optimum joint is lacking. The main novelty of this paper is the fact that it is the first time to use the response surface method (RSM) in conjunction with electron backscattered microscopy (EBSD) and transmission electron microscopy (TEM) for FSW of single phase brasses. Therefore, the aims of this study can be divided into two categories. The first aim was optimizing the FSW parameters to enhance the tensile properties of the single phase brass joints. The second aim was elucidating the microstructure, substructure, and texture of the optimized joint.

2. Materials and methods

Single phase brass (Cu–30 wt.% Zn) plates with dimensions of 100 mm × 100 mm × 2 mm were used as the base materials (BMs). A H13 hot work steel tool consisted of a shoulder with a diameter of 12 mm, and a pin with a diameter and length of respectively 3 mm and 1.75 mm was employed. For experimental design and optimizing aim, the response surface method (RSM) in conjunction with central composite rotatable design was used using Design Expert software. The considered parameters with their symbols, units, levels, and actual values are summarized in Table 1. In addition, the experimental design matrix including 20 runs, the experimental and predicted ultimate tensile strength (UTS) and elongation (E) is summarized in Table 2.

The microstructure of the joints was first examined by using a light microscopy (LM). The LM specimens were cross sectioned from the joints perpendicular to the FSW direction, and they were then prepared by mechanical polishing and etching with a solution of 50 mL HCl, 10 mL H_2O and 5 g $FeCl_3$. The grain size of the joints were estimated by using the mean intercept method. In addition, tensile test was conducted to reveal the tensile properties of the joints. For this purpose, the longitudinal tensile samples were wire cut along the welding line with gage size of 12 mm (length), 3 mm (width), and 2 mm (thickness). The schematic of the tensile specimens with dimensions is illustrated in Fig. 1. Tensile tests were conducted at a stain rate of 1 mm/min. It is notable that four tensile tests were carried out for each FSW parameters.

A Philips XL30 E-SEM field emission gun scanning electron microscope equipped with EBSD system was employed for OIM of the joint welded at optimum condition. The EBSD scans were taken from the center of the SZs of the joints. The

Table 1 – Coded and actual values of FSW parameters.

Parameters	Unit	Levels				
		−1.68	−1	0	1	1.68
Rotational speed (A)	rpm	463	600	800	1000	1136
Traverse speed (B)	mm/min	16	50	100	150	184
Axial force (C)	kN	1.66	2	2.5	3	3.34

Table 2 – Design layout including experimental and predicted values.

No.	Run	Coded values of parameters			UTS (MPa)		Elongation (%)	
		(A)	(B)	(C)	Experimental	Predicted	Experimental	Predicted
1	20	−1	−1	−1	312	309	36	37
2	6	1	−1	−1	299	290	42	45
3	17	−1	1	−1	315	319	27	25
4	4	1	1	−1	272	272	30	31
5	15	−1	−1	1	281	284	48	48
6	18	1	−1	1	318	318	52	56
7	2	−1	1	1	282	294	44	42
8	13	1	1	1	293	300	48	48
9	11	−1.68	0	0	302	305	34	33
10	1	1.68	0	0	291	295	48	45
11	9	0	−1.68	0	286	294	56	53
12	8	0	1.68	0	299	288	32	36
13	19	0	0	−1.68	298	306	29	30
14	3	0	0	1.68	319	308	52	53
15	10	0	0	0	318	315	46	46
16	16	0	0	0	315	315	46	46
17	12	0	0	0	315	315	46	46
18	14	0	0	0	315	315	46	46
19	7	0	0	0	313	315	46	46
20	5	0	0	0	310	315	46	46

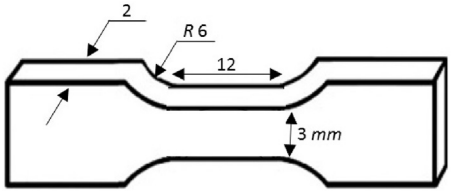

Fig. 1 – Schematic illustration of the tensile specimens used in this study.

specimens for OIM were finalized after mechanical polishing by electropolishing for 30 s in a solution containing 250 mL H_3PO_4, 250 mL ethanol, 50 mL propanol, 500 mL distilled water, and 3 g urea at 10 V and 25 °C. TEM (JEOL JEM 2010) was used for more clarification of the microstructural details. For TEM sample preparation, the electrojet thinning was used by means of a solution including 30% H_3PO_4 and 70% distilled water at applied potential of 80 V. The TEM specimens were taken from the center of the SZs of the joints. Moreover, the fracture surfaces of the tensile samples were characterized scanning electron microscope.

3. Results and discussion

3.1. *Typical macrostructure*

The macrostructure of the joint had different microstructural zones of BM, thermomechanically affected zone (TMAZ), and SZ. It is notable that HAZ was not seen may be due to the high thermal conductivity of the brass. The BM had coarse equiaxed grains, which was due to its initial annealing process (Fig. 2a). In addition, the TMAZ had similar structures of deformed grains (Fig. 2b). In TMAZ, the grains have been elongated along the shear stresses induced by the rotational tool. In addition, due to the insufficient heat and deformation in TMAZ, the dynamic recrystallization (DRX) has not been occurred. Therefore, the deformed grains of the TMAZ have not undergone the DRX, and hence their elongated and deformed morphology has not changed to the fine and equiaxed one. On

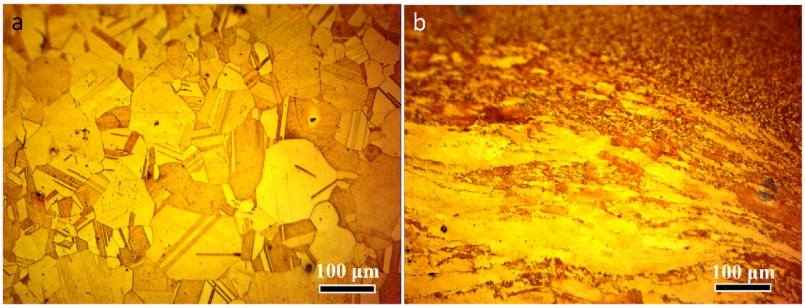

Fig. 2 – The microstructures of the (a) BM, and (b) transition area between BM and SZ of the joint number 10 showing both TMAZ and SZ.

Table 3 – ANOVA table for response UTS.

Source	Sum of squares	Degree of freedom	Mean square	*F*-value	*P*-value	
Model	3295.07	9	366.12	14.73	0.0017	Significant
A	137.4	1	137.4	10.78	0.0022	
B	50.02	1	50.02	8.65	0.024	
C	9.38	1	9.38	6.12	0.0349	
AB	392	1	392	5.07	0.0481	
AC	1352	1	1352	17.48	0.0019	
BC	0	1	0	0	1	
A^2	401.6	1	401.6	5.19	0.0459	
B^2	1031.65	1	1031.65	13.34	0.0044	
C^2	113.31	1	113.31	1.46	0.254	
Residual	773.48	10	77.35			
Lack of Fit	738.15	5	147.63			
R^2	0.9099					
Adjusted R^2	0.888					

the other hand, the SZ have contained fine equiaxed grains, which shows the occurrence of DRX (Fig. 2b).

3.2. *Effect of FSW parameters on tensile strength*

The effect of FSW parameters was studied using mathematical models developed by RSM, which is well described in literature [16–18]. In addition, the analysis of variance (ANOVA) was used to explore the significance of the models. The ANOVA data are summarized in Tables 3 and 4. The R^2 and adjusted R^2 values for UTS and *E* were 0.90–0.87 and 0.93–0.88, respectively. Thus, the models can predict the UTS and *E* of the joints, accurately. In addition, the *F*-value and *P*-value in ANOVA data can be used for determining the effectiveness of the parameters. The smaller *P*-value and larger *F*-value indicate more significant model parameters [18]. In the case of UTS, for rotational speed (A), traverse speed (B), and axial force (C), the *P* and *F* values were 0.002–10.78, 0.02–8.65, and 0.03–6.12, correspondingly. Therefore, the order of the effective parameters on the UTS is as follows: A > B > C. This means that the rotational speed and axial force had the highest and lowest effect on the UTS. In the case of E, for rotational speed (A), traverse speed (B), and axial force (C), the *P* and *F* values were 0.001–18.37, 0.0002–34.84, and <0.0001–66.84, correspondingly. Thus, the axial force had the highest effect on the *E*, where rotational speed had the lowest effect.

Moreover, the counter and perturbation plots for the UTS of the joints is shown in Fig. 3. Perturbation plot illustrates the effect of the parameters on the UTS or E, when the other parameters are set constant. According to Fig. 3, by increasing the tool rotational speed, the UTS value increases up to a maximum amount and then decreases. At lower rotational speeds due to insufficient heat and material flow, defects were formed on the advancing side of the joints, which cause lower UTS amounts. For instance, the defect formed in the joint number 7 (experiment number 7 in Table 2) is illustrated in Fig. 4.

At higher rotational speeds, the high heat input resulted in grain growth in the joints. For example, the microstructures of the joints welded at conditions of experiment number 1 and 2 are shown in Fig. 5. By increasing the rotational speed from experiment number 1 to number 2, the average grain size was increased. The effect of axial force was similar to the effect of the rotational speed in Fig. 3. For more details of the axial force effect, the joints welded at conditions of experiments number 4 and 8 can be compared. In experiment number 4, due to low axial force, the material plastic deformation was inadequate, and hence the void were formed in the cross section of the joint as shown in Fig. 6. On the other hand, when the axial force was large, the grain were grown in the SZ, as shown in Fig. 7. The effect of traverse speed was opposite of the rotational speed. At lower traverse speeds, the larger grain

Table 4 – ANOVA table for response Elongation.

Source	Sum of squares	Degree of freedom	Mean square	*F*-value	*P*-value	
Model	1342.74	9	149.19	15.19	0.0001	Significant
A	180.4	1	180.4	18.37	0.0016	
B	342.21	1	342.21	34.84	0.0002	
C	656.41	1	656.41	66.84	<0.0001	
AB	2	1	2	0.2	0.6614	
AC	0	1	0	0	1	
BC	18	1	18	1.83	0.2056	
A^2	107.18	1	107.18	10.91	0.008	
B^2	5.29	1	5.29	0.54	0.4799	
C^2	48.96	1	48.96	4.99	0.0496	
Residual	98.21	10	9.82			
Lack of Fit	98.21	5	19.64			
R^2	0.9318					
Adjusted R^2	0.8805					

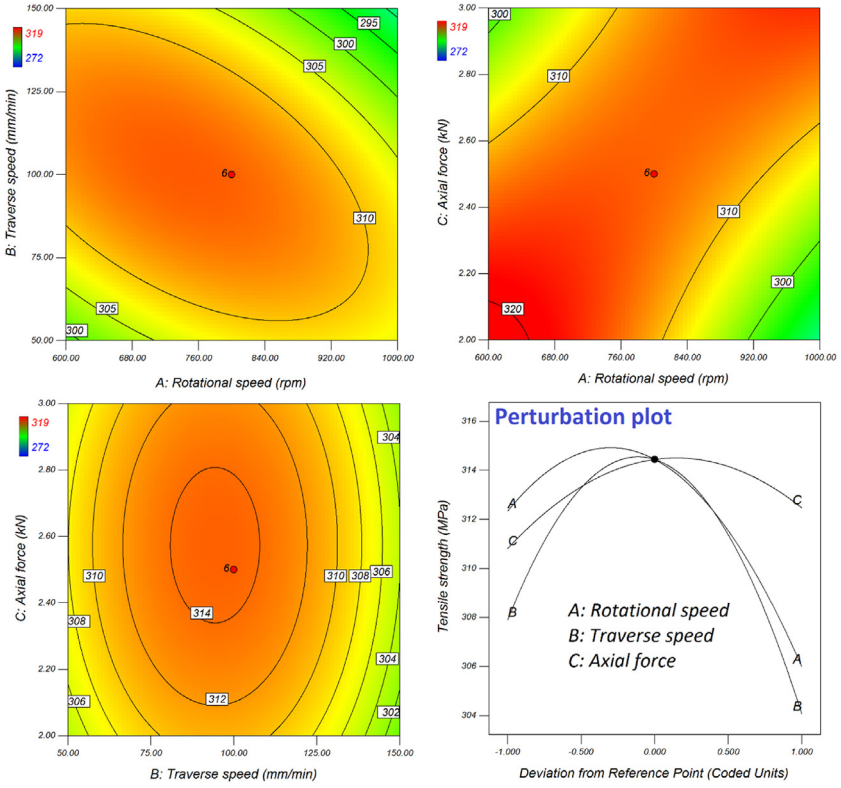

Fig. 3 – The contour and perturbation plots for the UTS.

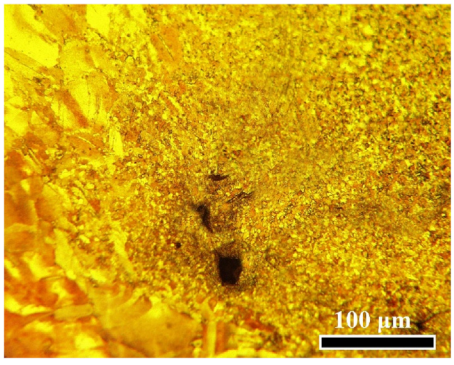

Fig. 4 – The microstructure of the advancing side in TMAZ of the joint number 7 showing the formation of the defects.

sizes were the reason of the lower UTS values, where at higher traverse speeds, the voids were formed.

It is well accepted that the grain size (d) of the materials subjected to the thermomechanical processes is a reverse function of the Zener–Holloman (Z) parameter as follows [19]:

$$d = aZ^b, Z = \epsilon' \exp\left(\frac{Q}{RT}\right) \rightarrow \ln d = \ln a + b \ln\left(\epsilon' \exp\left(\frac{Q}{RT}\right)\right) \quad (1)$$

In Eq. (1), the a and b are the constants, ε' is strain rate, Q stands for the deformation activation energy, R refers to the gas constant, and T belongs to the deformation temperature. The ε' and T can be formulated as Eq. (2) and Eq. (3) as follows [20]:

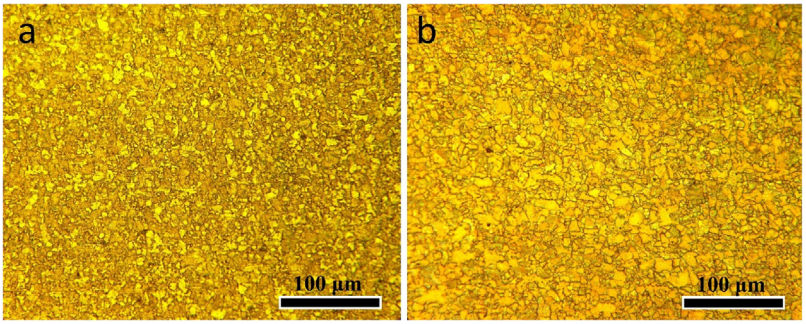

Fig. 5 – The microstructure of the joints welded at lower heat input or experiment number 1 (a) and higher heat input or experiment number 2 (b).

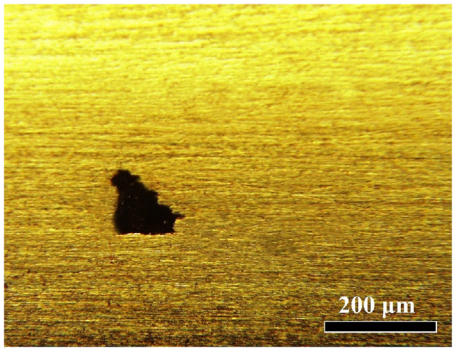

Fig. 6 – The macrostructure of the advancing side in TMAZ of the joint number 4 showing the formation of the void.

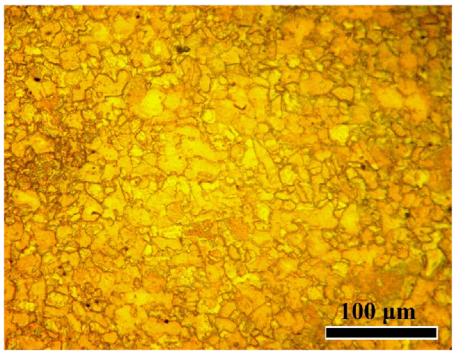

Fig. 7 – The microstructure of the joint welded at the condition of the experiment number 8.

$$\epsilon' = \frac{\omega \pi r_e}{L_e} \tag{2}$$

$$\frac{T}{T_m} = k^2 \left(\frac{\omega^2}{10^4 . \vartheta} \right)^{\alpha} \tag{3}$$

In Eq. (2), ω, r_e, and L_e represent the rotational speed, effective radius and depth of the dynamically recrystallized zone, respectively. In Eq. (3), k and α are constant, T_m denote the melting temperature, and ϑ is tool traverse speed. From Eqs. (1)–(3), three major outcomes can be summarized. First, the effect of rotational speed is more than the traverse speed. Second, by increasing the traverse speed, the temperature decreases, which cause larger Z values, and hence it leads to smaller d. Third, by increasing the tool rotational speed both of the strain rate and temperature increase, which have the inverse effect on the Z. Larger strain rates result in larger Z, where the high temperatures cause smaller Z. This shows that during FSW strain rate and temperature are competing parameters for controlling the final grain size. In this study, continuously increase in grain size by increasing the rotational speed reveals that the temperature parameter is dominant factor. This confirms that why the model predicted that the rotational speed was the most effective parameter on the UTS.

3.3. *Effect of FSW parameters on elongation*

The effect of welding parameters on the E of the joints is shown in Fig. 8 using contour and perturbation plots. Form

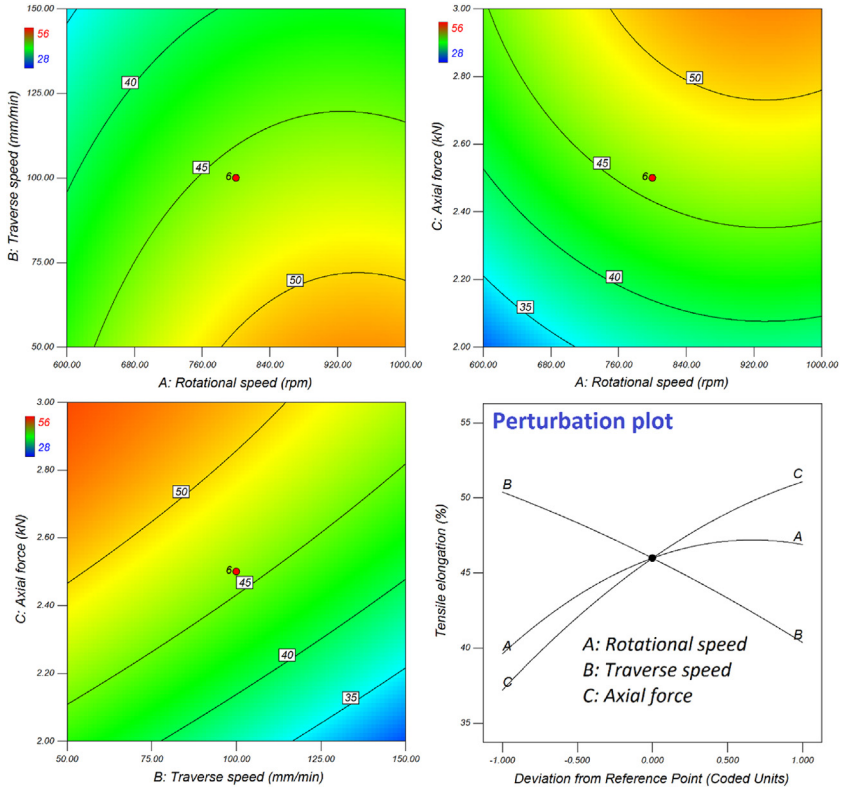

Fig. 8 – The contour and perturbation plots for the E.

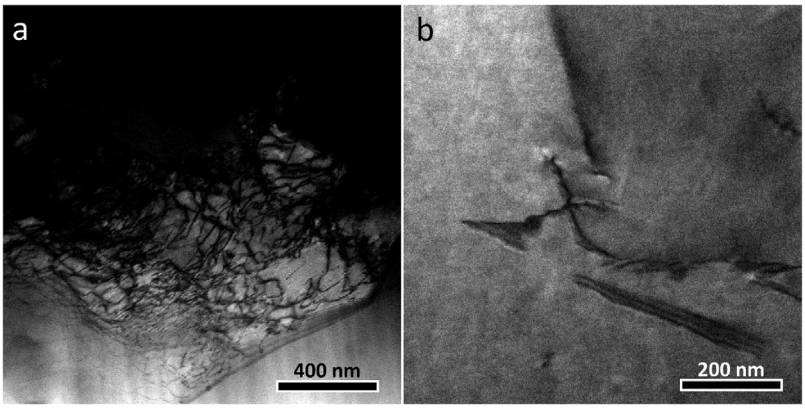

Fig. 9 – The TEM images of the SZs in the joints welded at lower heat input (a) and higher heat input (b).

Fig. 8, by increasing rotational speed and axial force or by decreasing traverse speed, the E of the joints was increased, continuously. This effect is not consistent with the fact that finer grain sizes cause larger elongation. Thus, there should be other metallurgical phenomena. According to the TEM results for the joints of the experiments number 1 and 2 as shown in Fig. 9, the dislocation density was lower in the joint number 2 compared to number 1. Therefore, despite the larger grain size in the joint number 2, the lower dislocation density causes more *E* compared to that of the joint number 1. It is worthy to note that the fractography of the tensile samples of the joint number 1 and 2 confirmed this effect. The SEM images of the fracture surfaces of the joint number 1 and 2 are illustrated in Fig. 10. From Fig. 10, the fracture surface of the joint number 2 had more and finer dimples compared to that of the joint number 1.

3.4. *Optimizing the parameters*

The optimum condition for achieving the maximum UTS and maximum *E* values was predicted by the models in Design Expert software. The optimizing result showed that the maximum UTS value of 318.6 MPa and maximum *E* amount of 54.9% can be achieved by FSW at a rotational speed, traverse speed, and axial force of 1000 rpm, 58 mm/min, and 3 kN, respectively. It is considerable that this optimum condition was predicted to simultaneous enhancement of the UTS and *E* of the joints.

3.5. *Strengthening mechanisms*

In this section, the strengthening mechanisms which cause higher UTS amounts in lower heat input conditions have been discussed. For this aim, the microstructural aspects of the two joints welded at lower (experimental number 3) and higher (experimental number 9) heat inputs are considered. The different strengthening mechanisms can be responsible for the higher UTS of the low heat input joint (number 3), which is strongly influenced by microstructural evolution during FSW. It is well documented that the strength of the polycrystalline metals depends on the values of different strengthening items such as the grain boundary strengthening ($\Delta\sigma_{gb}$), the solution strengthening ($\Delta\tau_{ss}$), the dislocation strengthening ($\Delta\tau_{D}$), the precipitation strengthening ($\Delta\tau_{ppt}$), and the strengthening due to the texture which is usually defined by Taylor factor [13,21]. Because the brass used in this study does not contain

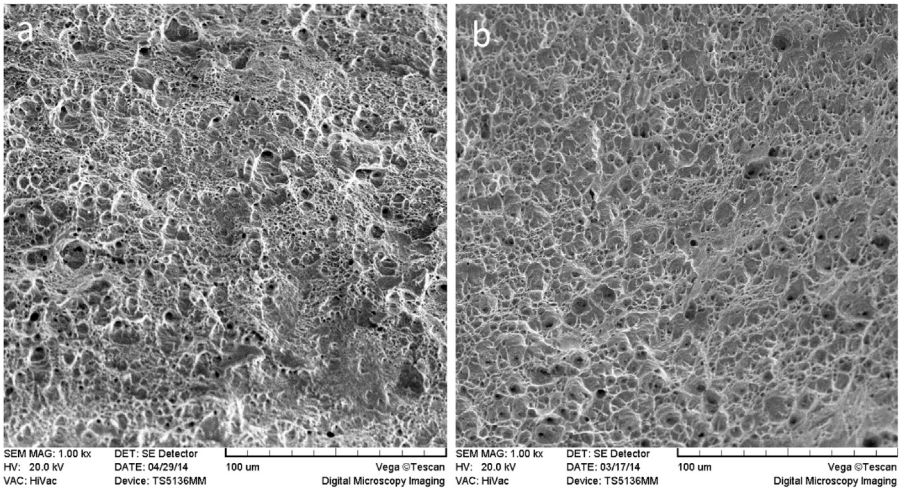

Fig. 10 – SEM images of the fracture surfaces for the joints welded at (a) lower heat input and (b) higher heat input.

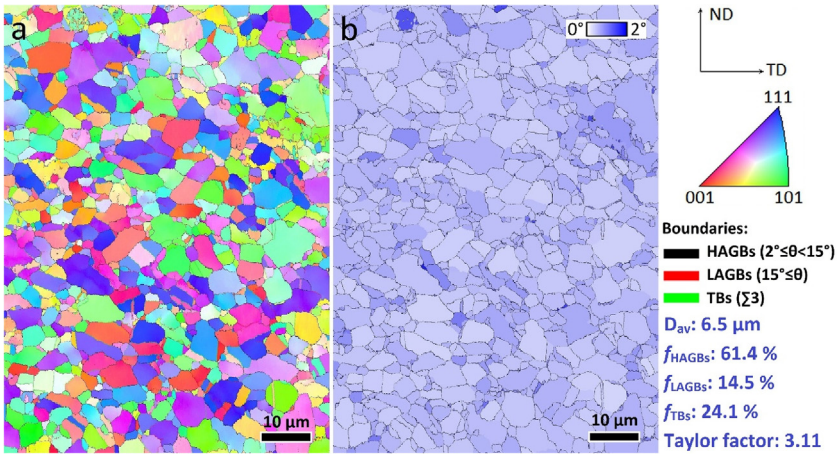

Fig. 11 – OIM data for the joint welded at the lower heat input (joint number 3). (a) Inverse pole figure (IPF) map in conjunction with grain boundaries (GBs), (b) grain average misorientation (GAM) map in conjunction with data for the amounts of high angle grain boundaries (HAGBs with $\theta \geq 15^{\circ}$), low angle grain boundaries (LAGBs with $2^{\circ} < \theta < 15^{\circ}$), twin boundaries (TBs), average grain size (D_{av}), and Taylor factor. The HAGBs, LAGBs, and the TBs are marked by black, red, and green colors in GBs map, correspondingly.

precipitates, thus the strengthening mechanisms will as follows: $\Delta\sigma_{gb}$, $\Delta\sigma_{ss}$, $\Delta\tau_{D}$, and effect of texture. Among the mentioned strengthening mechanisms only the $\Delta\sigma_{gb}$, $\Delta\tau_{D}$, and M can be affected by the microstructural mechanisms during FSW.

The OIM data for the low and high heat input joints are illustrated in Figs. 11 and 12, respectively. The low heat input joint had an average grain size of 6.5 µm (Fig. 11), which was finer than that of the high heat input joint i.e. 10.2 µm (Fig. 12). In addition, the HAGBs in the low heat input joint were 85.5% of the total grain boundaries (Fig. 11), where in the case of the high heat input joint, it has been reduced to 78.8% (Fig. 12). In addition to the finer grain sizes in the low heat input joint compared to the low heat input joint, the amount of HAGBs has been increased.

These HAGBs act as the obstacles against the dislocation movement, and hence cause higher $\Delta\sigma_{gb}$ [22]. The origin of finer grains and larger amount of HAGBs in the low heat input joint can be attributed to the microstructural evolution during FSW. Mironov et al. [10] have shown that the mechanism of the grain structure formation during FSW of the 70/30 brass does not depend on the heat input. They showed that in a wide range of parameters, the discontinuous dynamic recrystallization (DDRX) is the only mechanism governing the grain structure formation. It is well documented that DDRX cause formation of new grains with different texture, which leads to destroy the deformation texture of the materials or to lower texture intensity [23].

According to the pole figures (PFs) for the low and high heat input joints, which are illustrated in Fig. 13, the texture type in

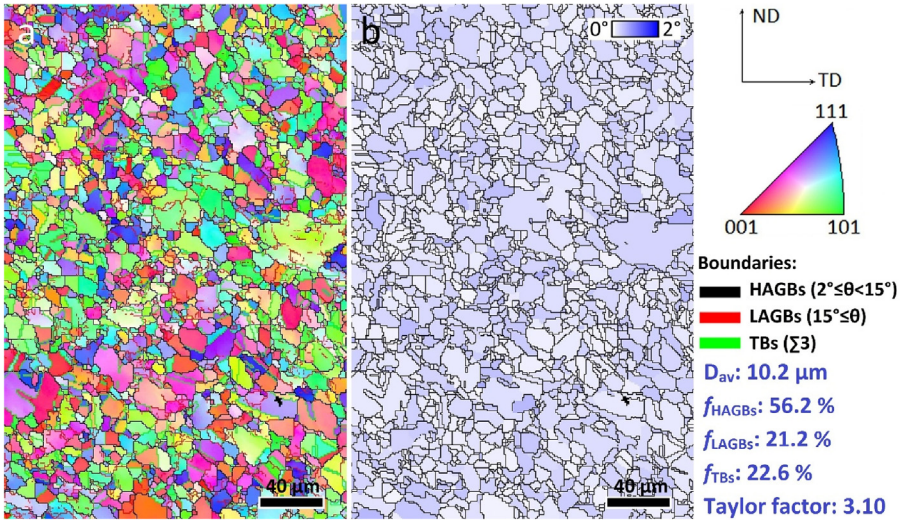

Fig. 12 – OIM data for the joint welded at the lower heat input (joint number 9). The description of the (a and b) is the same with Fig. 8.

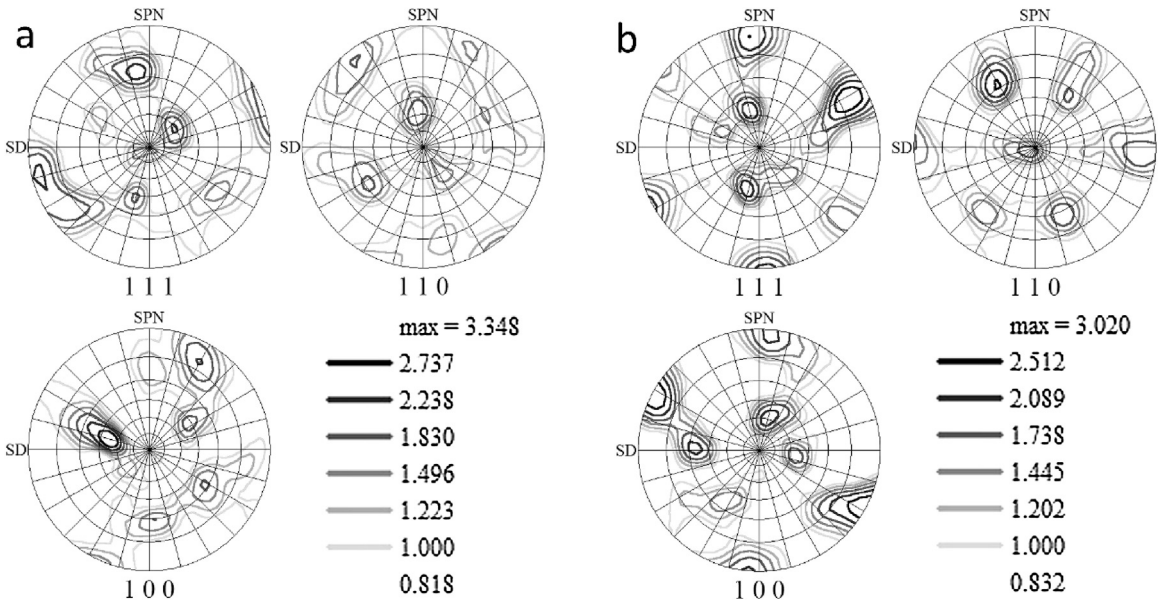

Fig. 13 – The (111), (110), and (100) PFs: (a) for the joint welded at the lower heat input condition or experiment number 3, and (b) for the joint welded at the higher heat input condition or experiment number 9.

both of the joints were shear texture. In addition, the texture intensity for them are approximately equal. Thus, the DDRX cannot be the reason of the different grain sizes. It seems that lower heat input during FSW of joint number 3 causes the lower peak temperature in the SZ of the joint, and hence it leads less grain growth after DDRX.

By increasing the dislocation density, the $\Delta\sigma_D$ increases, and hence the higher strength will be reached [24]. According to the GAM maps (see Figs. 11b and 12b) of the low and high heat input joints, the GAM values are higher in low heat input joint compared to the joint number 9. When the GAM values are larger, it means that the structure is more deformed, and hence the dislocation density in more [25]. This means that the structure in SZ of the low heat input joint was more deformed with higher dislocation densities.

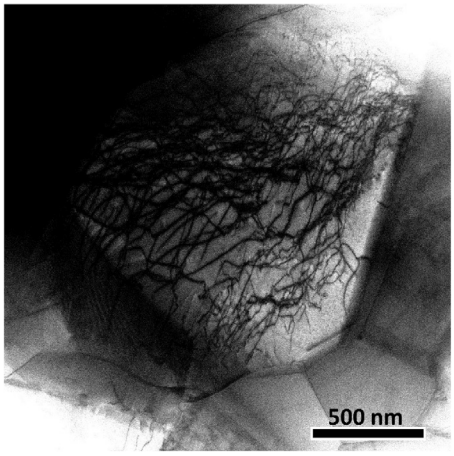

Fig. 14 – The TEM image of the joint welded at the lower heat input condition or experiment number 3.

Similarly, TEM image of the SZ in the low heat input joint (see Fig. 14) showed a high dislocation density. In fact, the higher heat input during FSW cause higher temperatures, and hence it leads to higher dislocation mobility, which results in the recovery of the dislocations. Therefore, in low heat input joint due to higher dislocation density, the $\Delta\sigma_n$ parameter is higher than that of the high heat input joint, and hence it causes higher UTS.

The effect of texture on the strength occurs as the Taylor factor. The higher Taylor factor causes higher strength. The Taylor factors for the low and high heat input joints were 3.11 and 3.10, respectively. Thus, it seems that the texture had a negligible effect on the strength value. In summary, the main strengthening mechanisms causing higher UTS values in low heat input joint were the grain boundary and dislocation mechanisms.

4. Conclusions

In this study, the RSM was used to evaluate the effect of bead on plate FSW parameters on the tensile properties of the single phase brass plates, and the microstructural features were analyzed using EBSD, TEM, and SEM. The following conclusions can be summarized. By increasing the FSW parameters, the UTS of the joints increases up to a maximum value and then decreases due to the formation of defects in lower heat inputs and grain growth at higher heat inputs. The elongation of the joints increases continuously by increasing rotational speed and axial force and decreasing the traverse speed due to elimination of defects at higher heat inputs and reduction of dislocation density. The most effective parameters on the UTS and elongation of the joints are tool rotational speed and axial force, respectively. By FSW at a

rotational speed, traverse speed, and axial force of 1000 rpm, 58.4 mm/min, and 3 kN, the maximum value of 318.5 MPa and 54.9% can be obtained for UTS and elongation of the joints. At lower heat input conditions, finer grains, more HAGBs, higher dislocation densities, larger Taylor factors, and higher texture intensities are formed compared to the higher heat input conditions. The main strengthening mechanisms which cause higher UTS in the joints welded at lower heat input conditions are grain boundaries and dislocation densities.

REFERENCES

[1] G. Çam, H.T. Serindağ, A. Çakan, S. Mistikoglu, H. Yavuz, The effect of weld parameters on friction stir welding of brass plates, Materialwissenschaft und Werkstofftechnik 39 (6) (2008) 394–399.

[2] I. Galvão, R.M. Leal, D.M. Rodrigues, A. Loureiro, Influence of tool shoulder geometry on properties of friction stir welds in thin copper sheets, J. Mater. Process. Technol. 213 (2) (2013) 129–135.

[3] C. Meran, The joint properties of brass plates by friction stir welding, Mater. Design 27 (9) (2006) 719–726.

[4] H.S. Park, T. Kimura, T. Murakami, Y. Nagano, K. Nakata, M. Ushio, Microstructures and mechanical properties of friction stir welds of 60% Cu–40% Zn copper alloy, Mater. Sci. Eng. A 371 (1–2) (2004) 160–169.

[5] G. Çam, Friction stir welded structural materials: beyond Al-alloys, Int. Mater. Rev. 56 (1) (2011) 1–48.

[6] A.M.A. Heidarzadeh, E. Nazari, H. Khodaverdizadeh, K. Rabei, Developing Empirical Relationships to Predict Tensile Strength, Elongation and Hardnesss of Friction Stir Welded Pure Copper Joints 3rd International Conference on Manufacturing Engineering, 2011.

[7] A. Heidarzadeh, T. Saeid, A comparative study of microstructure and mechanical properties between friction stir welded single and double phase brass alloys, Mater. Sci. Eng. A 649 (2016) 349–358.

[8] Y.-F. Wang, J. An, K. Yin, M.-S. Wang, Y.-S. Li, C.-X. Huang, Ultrafine-grained microstructure and improved mechanical behaviors of friction stir welded Cu and Cu–30Zn joints, Acta Metall. Sin. (Engl. Lett.) (2018).

[9] A. Heidarzadeh, T. Saeid, Correlation between process parameters, grain size and hardness of friction-stir-welded Cu–Zn alloys, Rare Metals (2016) 1–11.

[10] S. Mironov, K. Inagaki, Y.S. Sato, H. Kokawa, Development of grain structure during friction-stir welding of Cu–30Zn brass, Philos. Mag. 94 (27) (2014) 3137–3148.

[11] G.M. Xie, Z.Y. Ma, L. Geng, Effects of friction stir welding parameters on microstructures and mechanical properties of brass joints, Mater. Trans. 49 (7) (2008) 1698–1701.

[12] G. Cam, S. Mistikoglu, M. Pakdil, Microstructural and mechanical characterization of friction stir butt joint welded 63% Cu–37% Zn brass plate, Weld. J. 88 (11) (2009) 225s–232s.

[13] A. Heidarzadeh, T. Saeid, V. Klemm, Microstructure, texture, and mechanical properties of friction stir welded commercial brass alloy, Mater. Charact. 119 (2016) 84–91.

[14] A. Ozer, A. Sik, B. Cevik, M. Ozer, The effect of friction stir welding parameters on microstructure and fatigue strength of CuZn37 brass alloys, Kovove Materialy-Metallic Materials 55 (2) (2017) 107–114.

[15] X.C. Liu, Y.F. Sun, T. Nagira, K. Ushioda, H. Fujii, Correction to: microstructure evolution of Cu–30Zn during friction stir welding, J. Mater. Sci. 53 (15) (2018), 11130-11130.

[16] A. Heidarzadeh, H. Khodaverdizadeh, A. Mahmoudi, E. Nazari, Tensile behavior of friction stir welded AA 6061-T4 aluminum alloy joints, Mater. Design 37 (0) (2012) 166–173.

[17] K. Elangovan, V. Balasubramanian, S. Babu, Predicting tensile strength of friction stir welded AA6061 aluminium alloy joints by a mathematical model, Mater. Design 30 (1) (2009) 188–193.

[18] A. Mohammadzadeh, M. Azadbeh, H. Danninger, New concept in analysis of supersolidus liquid phase sintering of alpha brass, Powder Metall. 58 (2) (2015) 123–132.

[19] R.S. Mishra, Z.Y. Ma, Friction stir welding and processing, Mater. Sci. Eng.: R: Reports 50 (1–2) (2005) 1–78.

[20] M.J. Starink, A. Deschamps, S.C. Wang, The strength of friction stir welded and friction stir processed aluminium alloys, Scr. Mater. 58 (5) (2008) 377–382.

[21] M.J. Starink, S.C. Wang, A model for the yield strength of overaged Al–Zn–Mg–Cu alloys, Acta Mater. 51 (17) (2003) 5131–5150.

[22] T. Sakai, A. Belyakov, R. Kaibyshev, H. Miura, J.J. Jonas, Dynamic and post-dynamic recrystallization under hot, cold and severe plastic deformation conditions, Progr. Mater. Sci. 60 (0) (2014) 130–207.

[23] S. Wang, Z. Zhu, M. Starink, Estimation of dislocation densities in cold rolled Al-Mg-Cu-Mn alloys by combination of yield strength data, EBSD and strength models, J. Microsc. 217 (2) (2005) 174–178.

[24] Y.Z. Tian, S. Gao, L.J. Zhao, S. Lu, R. Pippan, Z.F. Zhang, N. Tsuji, Remarkable transitions of yield behavior and Lüders deformation in pure Cu by changing grain sizes, Scr. Mater. 142 (2018) 88–91.